

Carbon nanotube forests as top electrode in electroacoustic resonators

Santiago Esconjauregui,^{*1} Taron Makaryan,² Teona Mirea,³ Mario DeMiguel-Ramos,³ Jimena Olivares,³ Yuzheng Guo,¹ Hisashi Sugime,¹ Lorenzo D'Arsié,¹ Junwei Yang,¹ Sunil Bhardwaj,⁴ Cinzia Cepek,⁴ John Robertson,¹ Enrique Iborra.³

¹Department of Engineering, University of Cambridge, CB3 0FA Cambridge, United Kingdom

²Faculty of Radiophysics, Yerevan State University, 0005 Yerevan, Armenia

³Escuela Técnica Superior de Ingenieros de Telecomunicación, Universidad Politécnica de Madrid, 28021 Madrid, Spain

⁴Istituto Officina dei Materiali - Laboratorio TASC, I-34149 Trieste, Italy

Abstract

We grow carbon nanotube forests on piezoelectric AlN films and fabricate and characterize nanotube-based solidly-mounted bulk acoustic wave resonators employing the forests as the top electrode material. The devices show values for quality factor at anti-resonance of ~ 430 , and at resonance of ~ 100 . The effective coupling coefficient is of $\sim 6\%$, and the resonant frequencies are up to ~ 800 MHz above those observed with metallic top electrodes. AlN promotes a strong catalyst-support interaction, which reduces Fe catalyst mobility, and thus enforces the growth of forests by the base growth mechanism.

There exists nowadays an increasing need of developing chemical sensors suitable for real-time detection of gaseous species^{1,2} (e.g. in breath-based diagnosis³ or in high-temperature engine combustion⁴). Among them, label-free gravimetric sensors, using acoustic wave technologies¹, are the most promising options. They offer real time detection and high sensitivity, and can be integrated into complex devices at a low cost. One of the most common types of these sensors is the high-frequency bulk acoustic wave resonators, which consist of a thin film piezoelectric material (typically AlN)^{5,6} sandwiched between two metallic electrodes (e.g. Mo, W, Au, or Pt) to which a microwave (RF) signal is applied.¹ To maximize the gravimetric sensing performance, the top electrode should exhibit low mass, as the sensor response is a detection of the electrode mass variation. It is also desirable to maximize the contrast between the acoustic impedances of the AlN film and those of the electrodes. This allows confining the acoustic energy in the AlN and hence improving the overall device performance. In this letter, we report the fabrication and characterisation of electroacoustic resonators using carbon nanotube (CNT) forests as top electrode.

One of the drawbacks of currently-used metallic top electrodes is their limited area for sensing. This, along with the fact that the mass density of aforementioned metals is high (10–20 g cm⁻³) and induces a high mass loading for the resonators, warrants the investigation of alternative materials such as nanotube forests. Unaligned, tangled tubes have already been suggested for similar applications, but the potentiality of forest highly-ordered morphology and nanotube vertical alignment remains unexplored.⁷⁻⁹ Forests exhibit not only high surface area, but also low mass densities (as low as ~0.10 g cm⁻³). They would allow a much lower mass loading for a resonator, even for tubes lengthening several tens of micrometers.¹⁰ The weight of the top electrode would thus become controllable by varying the area density, length, nanotube wall number.^{11,12} Additionally, as nanotubes can be easily functionalized,¹³⁻¹⁷ the top electrode could also serve as a sensing layer. These features envisage that forest integration into resonators would make vertically-aligned CNTs a suitable top electrode material also acting as a sensing layer.

The fabrication of nanotube-based resonators requires fully controlling CNT growth on AlN, but this material has been poorly investigated as nanotube catalyst support.¹⁸ Herein, we demonstrate forest growth directly on AlN by chemical vapour deposition (CVD) in a simple processing step, and explain why this is possible. Using these forests, we fabricate nanotube-based, solidly-mounted bulk acoustic wave resonators. We study their resonant characteristics and determine values for quality factor at anti-resonance, Q_a , of ~430, and at resonance, Q_r , of around 100. The effective coupling coefficient, k_{eff}^2 , is of around 6%, and

the resonant frequencies, f_r , are up to ~800 MHz above those observed with metallic top electrodes and the same piezoelectric film thicknesses.

To obtain these results, we fabricate resonators with an AlN film (100 nm thick) deposited on an acoustic reflector in order to minimize the losses of acoustic energy to the substrate.¹⁹ The substrate is Si(100) coated with its native oxide. Figure 1a shows a typical cross-section scanning electron microscopy (SEM) view of a solidly-mounted resonator with the top electrode made of forests. The reflector consists of five alternating layers of SiO₂ (450 nm) and Mo (520 nm), low and high acoustic impedance materials respectively. The thickness of each layer of the reflector is a quarter of wavelength ($\lambda/4$), being the wavelength the ratio of the sound velocity in the film and the working resonant frequency. The thickness is adjusted for a reflection band centred at a frequency of ~2.5 GHz for longitudinal mode. The bottom electrode is an evaporated film of Ir (120 nm). The catalyst (1 nm Fe) is deposited on patterned areas of the AlN, which define the nanotube-based top electrode (height ~50 μm), as shown in Figure 1(b). The modulus of impedance at different frequencies is plotted in Figure 1(c). The resonators yield a repeatable electrical response, similar to devices with metallic top electrodes. To extract the parameters of the devices, we fit the values following the Mason's model (i.e. we evaluate the propagation of acoustic waves through a layered structure considering reflections due to acoustic impedances mismatches and the wave interaction with the piezoelectric layer).²⁰ The quality factor values at resonant and anti-resonant frequencies are assessed by fitting the electrical impedance responses of the resonators with the modified Butterworth van Dyke model.²¹ For their calculation, we use:

$$\begin{aligned} Q_r &\approx \frac{\omega_r L_m}{R_s + R_m} \\ Q_a &\approx \frac{\omega_a L_m}{R_0 + R_m}, \end{aligned} \quad (1)$$

where ω_r and ω_a are the resonant and anti-resonant angular frequencies, L_m is the motional inductance, and R_s , R_m , and R_0 are the series, motional, and loss resistances. The effective coupling coefficient is calculated using:

$$k_{eff}^2 = \frac{\pi f_r}{2 f_a} \left[\tan\left(\frac{\pi f_r}{2 f_a}\right) \right]^{-1}, \quad (2)$$

where f_a is the anti-resonant frequency. The devices achieve k_{eff}^2 in the range of ~6%. The typical f_r value is found to be ~3500 MHz. This value is about 800 MHz above of that found using metallic top electrodes and same AlN thickness. At this f_r , we determine Q_a values of about 430 and Q_r values of up to 100. Finally, the series resistance, R_s , averages values of

~33 Ω . The 800 MHz shift is strongly correlated to the geometry of the device (mainly the thickness of the piezoelectric layer and those of the electrodes) as well as to the properties of the electrode materials. In comparison to metallic electrodes (active area is 2500 μm^2), the active area of the forest top electrode (3-walled tubes, 7 nm diameter, 50 μm length, and area density of 5×10^{11} CNTs cm^{-2}) has increased up to seven orders of magnitude, whilst the electrode weight has diminished up to 3-fold, regardless of the fact that the electrode height changes from 120 nm (e.g. Mo) to 50 μm (nanotubes). Both active area and electrode mass can be further scaled by varying the properties of the tubes (area density, wall number, length, and tube diameter).²²⁻²⁴ Additionally, as the tubes can easily be chemically functionalized,²⁵ a forest top electrode could bond targeted species, which would allow dramatically enhancing the selectivity of a sensor. This would increase the possibilities of label-free gas detection (biological or non-biological species) depending of the designed affinity reaction.

The overall results suggest our devices are useful for the manufacturing of gravimetric sensors. The k_{eff}^2 value of ~6% is comparable with those obtained using a Mo or Ir top electrode. However, for fully integrating CNTs top electrode, the R_S should be lowered, close to that of ~2 Ω observed for metals. High resistive electrodes introduce high R_S and, consequently, worsen Q_r and make the frequency detection more difficult (since Q_r is inversely proportional to R_S , Eq.1). Herein, the relatively high values of R_S are related to the high sheet resistance of the tubes. It may be improved by increasing the nanotube area density, although this may also influence the electrical static capacitance of the devices.²⁶ Higher area densities will also improve Q_a , which currently average ~650 for metallic electrodes. Another option to reduce R_S could be to deposit a conductive interlayer on top of AlN. Several metals and compounds (e.g. W, Ir, Mo, TiSiN, doped-Si)²⁷⁻³⁰ allow direct forest growth, and so would reduce the contact resistance while the electrode weight is still low.

Further growth investigations prove it is feasible to tailor forest properties. Forest growth optimization will lead to the required values of Q_a , Q_r , and R_S . As Figure 2 shows, various thicknesses of Fe (0.4, 0.6, 0.8, 1.0, and 1.2 nm) yield forests over a wide range of CVD conditions (temperature: 650, 700, and 750 $^\circ\text{C}$, pressure: 1 bar of Ar:H₂ (1000:500 sccm), growth: 4, 7, or 10 sccm of C₂H₂ for 10 min), Figures 2(a)-(d). For instance, using 10 sccm of C₂H₂ at 650 $^\circ\text{C}$, the 0.8 nm Fe yields tubes of ~100 μm in length, Figures 2(a) and 2(c). At 700 $^\circ\text{C}$ but 4 sccm C₂H₂, 0.8 nm Fe yield longer tubes of ~300 μm , Figures 2(b) and 2(d). Transmission electron microscopy shows the tubes have a diameter of 12 ± 2 nm and 4-7

walls, inset of Figure 2(b). The nanoparticles formed at these two temperatures appear to have same dimensions and number density, Figures 2(e) and 2(f), suggesting the difference in tube length is related to growth conditions only. Using the weight gain method,¹⁰ we determine that the area density of the forests ranges from $1.2 \pm 0.1 \times 10^{11}$ CNTs cm^{-2} (0.5 nm Fe, 650 °C, 4 sccm C_2H_2) to $7.8 \pm 0.6 \times 10^{11}$ CNTs cm^{-2} (0.8 nm Fe, 750 °C, 4 sccm C_2H_2).

X-ray photoemission spectroscopy (XPS), with same set up and fitting procedures as previously reported,²⁷ reveals the growth of forests on AlN is related to Fe bonding N and Al which stabilizes the Fe nanoparticles, Figure 3. We argue this interaction is crucial to induce nanotube vertical alignment on AlN, and hence to grow tubes usable as top electrode in resonators. We analyse the samples after 1 nm Fe deposition and after 5, 20, 30 and 90 min vacuum annealing at 700 °C. For the as-deposited AlN samples coated with 1 nm of Fe ($t=0$), the Al $2p$ spectrum possesses three components: metallic Al (72.6 eV, red), AlN (73.6 eV, yellow), and Al_2O_3 , (74.6 eV, grey), Figure 3(a).³¹ The intensity of the AlN component is much greater than that of the oxide or the metallic components. After the deposition of 1 nm Fe, and subsequent annealing for 5, 20, 30, and 90 min, the total intensities decrease, which is expected due to Fe coverage. After annealing ($t=5$ or beyond), the metallic Al component is nearly vanished, but the other Al $2p$ lineshapes do not change significantly. Similar conclusions are withdrawn from the N $1s$ spectrum, Figure 3(b). As-deposited AlN and coated with 1 nm Fe shows three main components: NO (~ 400 eV, red) and AlO_xN_y (398.7 eV, green),³² and AlN (397.1 eV, yellow).³¹ After the first annealing ($t=5$), the oxides components nearly vanished and it appears a new component at 396.6 eV and associated to Fe-N (grey).³¹ This component reveals an interface reaction between Fe and AlN support. Both, the Al-N and the Fe-N components appear to be unaffected after annealing for 20, 30, or 90 min.

From the Fe $2p$ core level, it is also clear the interaction AlN-Fe at their contact interface, Figure 3(c). After 1 nm Fe deposition ($t=0$), the spectrum presents the Fe^{3+} (711.3 eV, solid green) and its satellite (718.9 eV, green stripes) components (related to ambient exposure). Upon annealing for 5, 20, 30 or 90 min, both components disappear and the spectra are now characterized by three new components: Fe^{+2} (710.6 eV, solid blue line), its satellite peak (715 eV, blue stripes), and Fe-N at 707 eV,³³ as already observed in the N $1s$ core level spectra. We note the Fe-N component increases with increasing the annealing time, and argue this component is responsible for nanoparticle stabilisation and inducement of nanotube vertical alignment and forest growth. Finally, the Fe reduction is also visible in the

O 1s spectra, Figure 3(d). The peak associated with Fe₂O₃ after deposition (~530 eV), vanishes after first annealing, while the component associated with FeO (~531.1 eV) tends to increase.

The nature of the AlN-Fe interaction is analogue to that in Al₂O₃-Fe. Having a comparable Pauli electronegativity (3.04 for N and 3.44 for O),³⁴ nitrogen atoms induce the stabilization of Fe via an Al-N-Fe covalent bonding (as determined by XPS and verified by long annealing times). A metal-nitrogen covalent bond can be formed either by π donation from the N to metals, or by σ -back donation from metal to nitrogen. It is also necessary a sufficient supply of *d*-orbitals unoccupied in the transition metal, which exists in high oxidation state. Two chemical configurations appear to be possible for this: Al-N-Fe and Al-N₂-Fe, but our XPS data shows Al-N-Fe is the predominant complex. This is likely related to the overlap of orbitals of nitrogen and metal.³⁵ N₂ has two unpaired electrons available in the π - and π^* -orbitals. However, the N-N π^* -bond becomes weaker upon interaction of metal and N₂ electronic orbitals. The metal-nitrogen-metal effectively stabilizes forming a polar covalent metal-nitrogen bond, which we argue stabilizes the catalyst nanoparticles on the AlN substrate.

We also prove nanoparticle stabilisation by interrupted growth.³⁶ After 0.7 nm Fe deposition and annealing, we flow 4 sccm of C₂H₂ for 1 min, stop for 10, and flow again for 10 min. The carbon source interruption creates a two-layer forest with a thicker layer at the bottom (due to longer growth time), Figure 4(a). The thin top layer (at the top) is the one grown for 1 min. These results confirm both nanoparticle Fe immobilisation on AlN and base growth mechanism of the tubes. Base growth mechanism assures a good mechanical adhesion and electrical contact between the forests and the AlN underneath. The surface energy of AlN plays a key role in the formation and stabilisation of Fe nanoparticles. By density functional theory calculations (same as previous),²⁹ we confirm that the surface energy of AlN is higher than that of Al₂O₃. We calculate the crystalline 1000 and amorphous surfaces using an ultra-soft pseudopotential with cut-off energy of 380 eV. The surface is cleaved from the Al-terminated <1000> direction because its surface energy is lower than that of N-terminated. To allow surface reconstruction, we use 2×2 and 3×3 supercells. A 15 Å thick vacuum is inserted to eliminate the image charge interaction. The slab thickness is 20 Å, which is enough to screen the interface interaction from each other. The central 10 Å slab part is fixed in order to simulate the bulk case. A 2×2×1 Monkhorst-Pack grid is used for integration in reciprocal space. These parameters give a total energy convergence of less than 0.01 eV. The

residual force is less than 0.02 eV \AA^{-1} for geometry optimization. While Al_2O_3 exhibits an average value of $\sim 100 \text{ meV \AA}^{-2}$, AlN shows a value of $\sim 189 \text{ meV \AA}^{-2}$, Figure 4(b). High surface energy supports minimize the interfacial energy by strongly bounding the particles.

In summary, we have demonstrated the fabrication of nanotube-top-electrode electroacoustic resonators. The performance is comparable to that obtained on devices consisting of two metallic electrodes, and it can further improved by optimizing the CNT properties. Forests can increase the active area of the electrode several orders of magnitude, decrease the mass loading by up to a factor of five, and could also be functionalized for selective sensing. Since AlN promotes a strong catalyst-support interaction, the Fe catalyst particles exhibit reduced mobility and the forests grow by the base growth mechanism. The devices are of potential use in chemical and biological gravimetric gas sensors and hence open up prospective applications of forests.

Acknowledgments

This work was partially supported by the European Commission through the project GRAFOL and the COST action IC1208 and by the Ministerio de Economía y Competitividad del Gobierno de España through project MAT2013-45957.

FIG 1. (a) Side-view SEM image of a solidly-mounted electroacoustic resonator with the top electrode made of a nanotube forest. (b) Optical image of a nanotube-based top electrode resonator. (c) Electrical responses of nanotube-based and metallic top electrode resonators.

FIG 2. Side-view SEM images of nanotube forests grown on AlN using 0.8 nm Fe. The growth conditions for (a) and (c) are 650 °C and 10 sccm of C₂H₂, while for (b) and (d) are 700 °C and 4 sccm of C₂H₂. (e) and (f) are respectively the seeding catalyst nanoparticles. Conditions for pretreatment are: 650 or 700 °C, 5 min in 1 bar Ar:H₂ (1000:500 sccm).

FIG 3. (a-d) are Al 2*p* , N 1*s*, Fe 2*p*, and O 1*s* XPS core level spectra. The spectra are collected in situ at 5, 20, 30, and 90 min of annealing (indicated at the right-hand side of each image).

FIG 4. (a) Interrupted growth conditions on AlN. The arrows indicate the interface separation between both periods of growth. (b) Atomic structure of (1000) Al-terminated AlN 2×2 reconstructed surface by DFT simulation (Al: pink, N: blue).

Figure 1

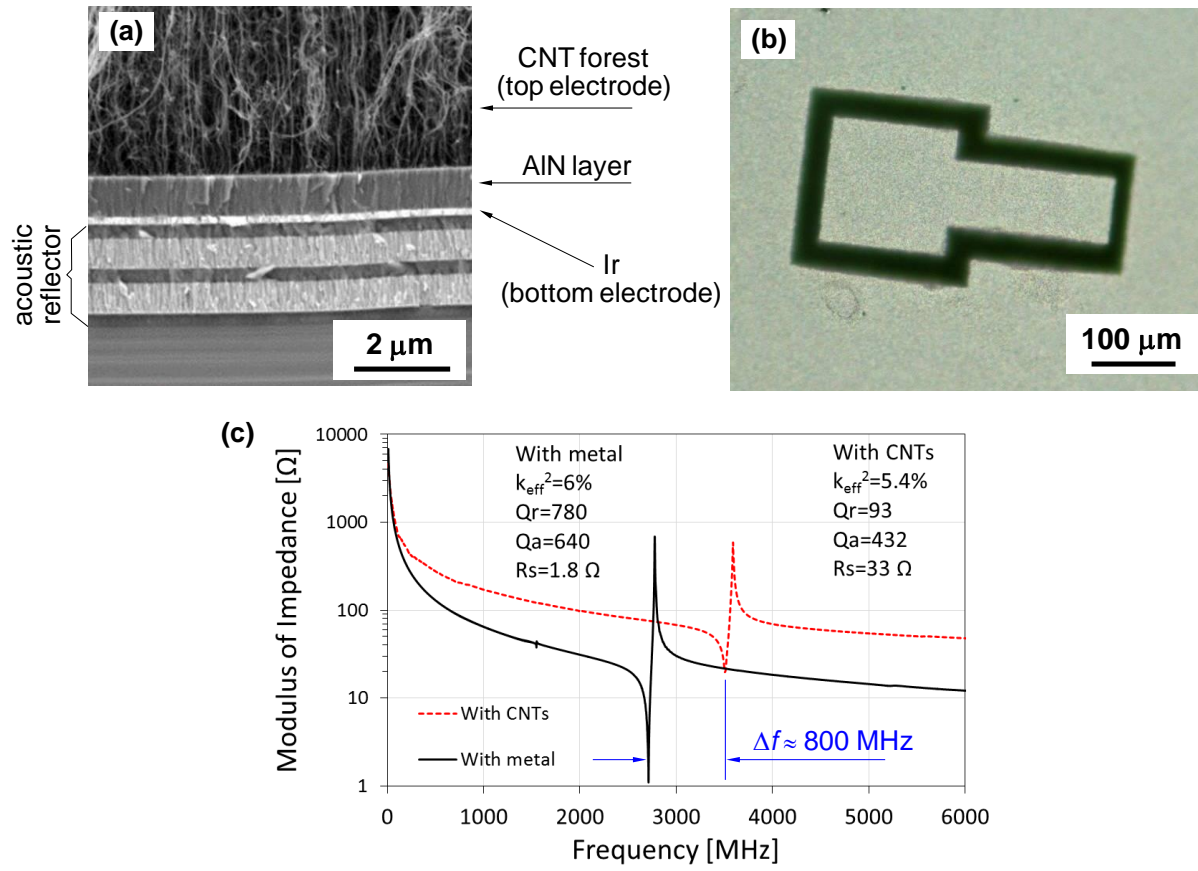


Figure 2

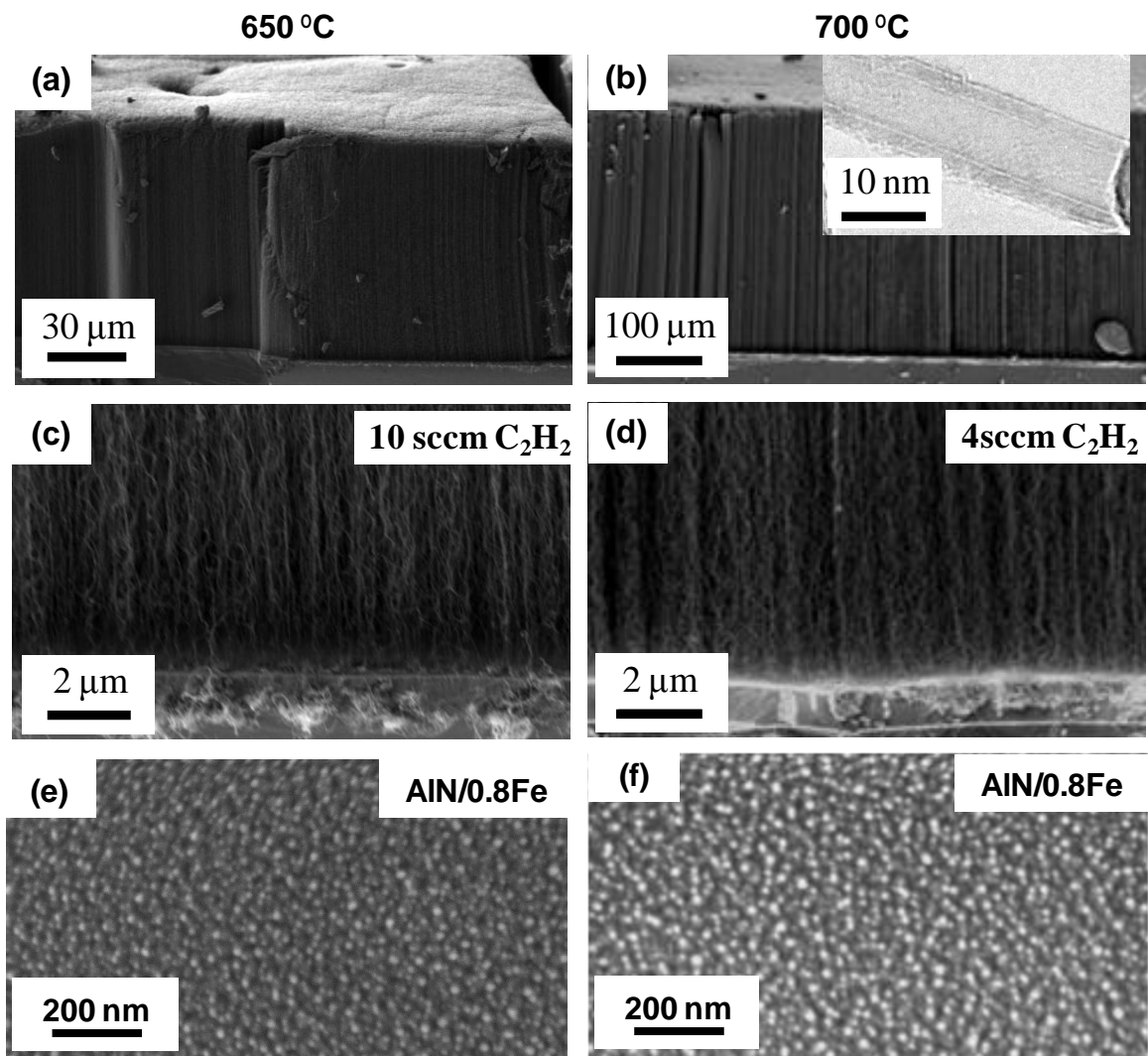


Figure 3

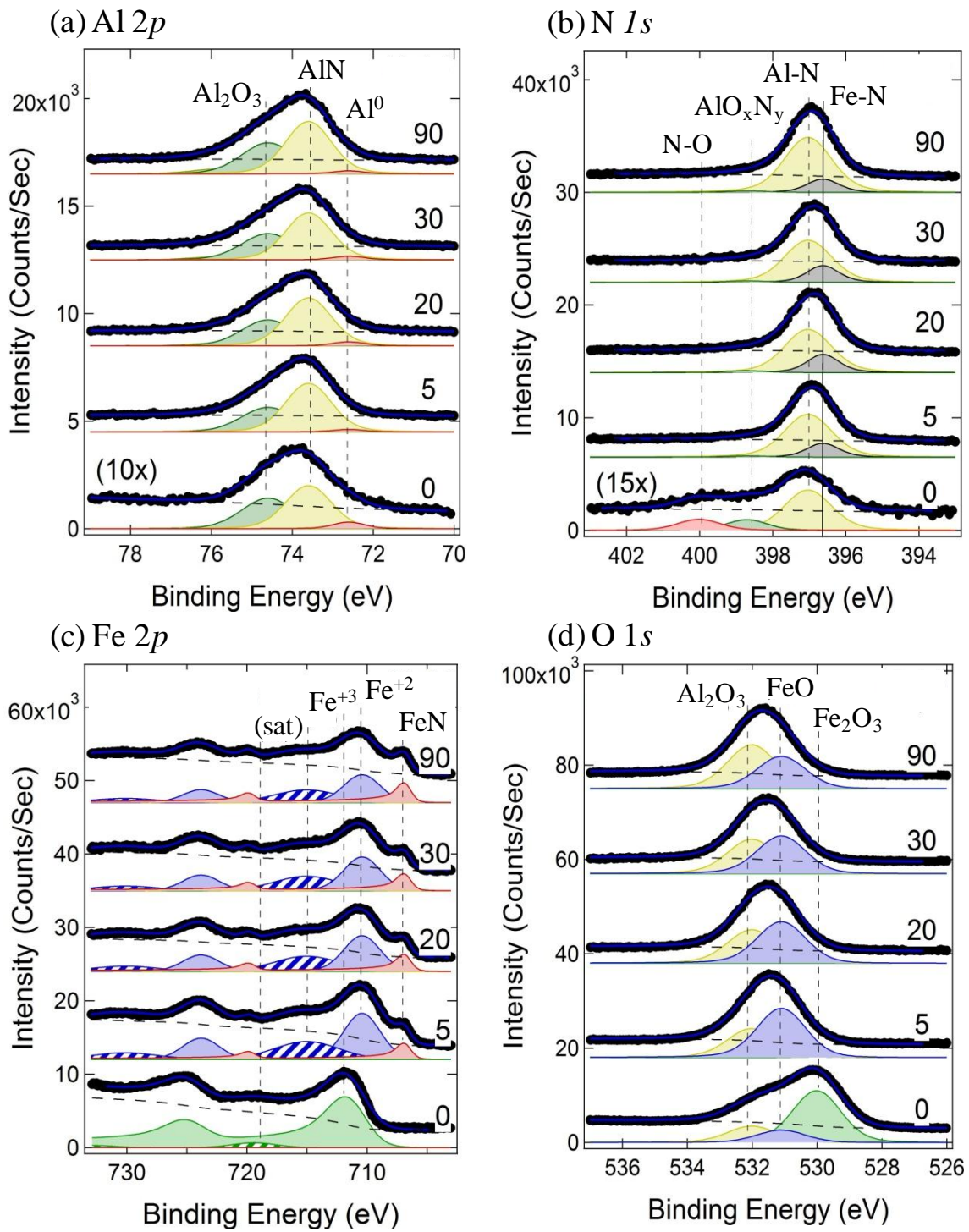
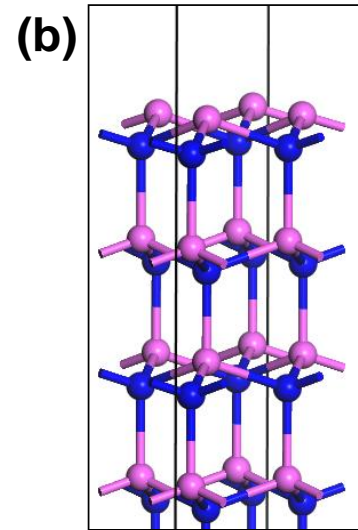
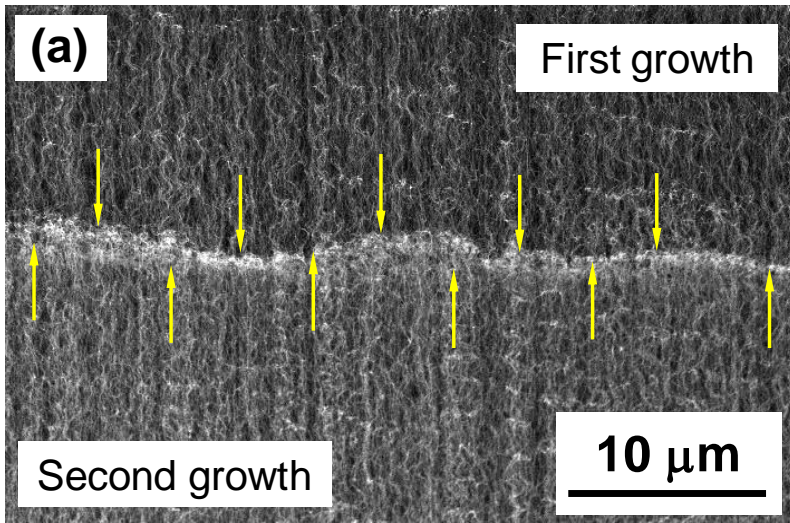


Figure 4



-
- 1 S. Fanget, S. Hentz, P. Puget, J. Arcamone, M. Matheron, E. Colinet, P. Andreucci, L. Duraffourg, Ed. Meyers, and M. L. Roukes, *Sensors & Actuact. B* 160, 804 (2011).
 - 2 W. Xu, S. Choi, and J. Chae, *Appl. Phys. Lett.* 96, 053703 (2010).
 - 3 N. Bu, N. Ueno, and O. Fukuda. *Sensors & Transducers Journal* 110, 131 (2009).
 - 4 M. Mittala and A. Kumara, *Sensors & Actuact. B* 203, 349 (2014).
 - 5 H.O. Loeb, M. Klee, C. Metzmacher, W. Brand, R. Milsom, and P. Lok, *Mat. Chem. & Phys.* 79, 143 (2003).
 - 6 G. Wingqvist, *Surf. & Coat. Technol.* 205, 1279 (2010).
 - 7 M. Rinaldi, C. Zuniga, N. Sinha, M. Taherie, G. Piazza, S. M. Khamis, and A.T. Johnson, *European Frequency and Time Forum & International Frequency Control* 443 (2008).
 - 8 L. García-Gancedo, Z. Zhu, E. Iborra, M. Clement, J. Olivares, A. J. Flewitt, W. I. Milne, G. M. Ashley, J. K. Luo, X. B. Zhao, and J. R. Lu, *Sensors & Actuact. B* 160, 1386 (2011).
 - 9 M. Dragoman, A. Muller, D. Neculoiu, D. Vasilache, G. Konstantinidis, K. Grenier, D. Dubuc, L. Bary, R. Plana, and E. Flahaut, *Appl. Phys. Lett.* 89, 143122 (2006).
 - 10 S. Esconjauregui, R. Xie, M. Fouquet, R. Cartwright, D. Hardeman, J. Yang, and J. Robertson, *J. Appl. Phys.* 113, 144309 (2013).
 - 11 B. Zhao, D. N. Futaba, S. Yasuda, M. Akoshima, T. Yamada, and K. Hata, *ACS Nano* 3, 108 (2009).
 - 12 C. R. Oliver, E. S. Polsen, E. R. Meshot, S. Tawfick, S. J. Park, M. Bedewy, and A. J. Hart, *ACS Nano* 7, 3565 (2013).
 - 13 C. Staii, M. Chen, A. Gelperin, and A.T. Johnson Jr, *Nano Lett.* 5, 1774 (2005).
 - 14 S. Dhalla, N. Jaggi, and R. Nathawat, *Sensors & Actuact. A: Physical* 201, 321 (2013).
 - 15 D. Bouilly, J. Cabana, F. Meunier, M. Desjardins-Carriere, P. Lapointe, P. Gagnon, F. L. Larouche, E. Adam, M. Paillet, and R. Martel, *ACS Nano* 5, 4927 (2011).
 - 16 D. R. Kauffman, D. C. Sorescu, D. P. Schofield, B. L. Allen, K. D. Jordan, and A. Star, *Nano Lett.* 10, 958 (2010).
 - 17 L. Lvova, M. Mastroianni, G. Pomarico, M. Santonico, G. Pennazza, C. Di Natale, R. Paolesse, and A. D'Amico, *Sensors & Actuact. B.* 170, 163 (2012).
 - 18 B. Eren, L. Marot, R. Steiner, T. de los Arcos, M. Düggelin, D. Mathys, K. N. Goldie, V. Olivieri, and E. Meyer, *Chem. Phys. Lett.* 609, 82 (2014).
 - 19 K. Lakin. *Ultrason. Symp. (IUS), Proceedings. 1995 IEEE*, 2, 905 (1995).
 - 20 J. Rosenbaum, *Bulk acoustic wave theory and devices* (Artech House, Boston 1988).

-
- 21 H. Jin, S.R. Dong, J.K. Luo, W.I. Milne, *Elect. Lett.* 47, 424 (2011).
- 22 W. Bauhofer and J. Z. Kovacs, *Compos. Sci. Tech.* 69, 1486 (2009).
- 23 L. Dai, D. W. Chang, J. B. Baek, and W. Lu, *Small* 8, 1130 (2012).
- 24 Z. Yuan, H-J. Peng, J-Q. Huang, X-Y. Liu, D-W. Wang, and Q. Zhang, *Adv. Funct. Mater.* 24, 6105 (2014).
- 25 Z. Zhu, L. García-Gancedo, A. J. Flewitt, H. Xie, F. Moussy, and W. I. Milne, *Sensors* 12, 5996 (2012).
- 26 E. Iborra, J. Sangrador, M. Clement, T. Mirea, M. DeMiguel-Ramos, J. Olivares, J. Capilla, L. García-Gancedo, S. Esconjauregui, A. J. Flewitt, and W. I. Milne, *European Frequency and Time Forum & International Frequency Control Symposium* 984 (2013).
- 27 S. Esconjauregui, C. Cepek, M. Fouquet, B. C. Bayer, A. D. Gamalski, B. Chen, R. Xie, S. Bhardwaj, C. Ducati, S. Hofmann, and J. Robertson, *J. Appl. Phys.* 112, 034303 (2012).
- 28 H. Sugime, S. Esconjauregui, J. Yang, L. D'Arzié, R. A. Oliver, S. Bhardwaj, C. Cepek, and J. Robertson, *Appl. Phys. Lett.* 103, 073116 (2013).
- 29 S. Esconjauregui, R. Xie, Y. Guo, S. Pfaendler, M. Fouquet, R. Gillen, C. Cepek, C. Castellarin-Cudia, Eslava, S. and J. Robertson, *Appl. Phys. Lett.* 102, 113109 (2013).
- 30 J. Olivares, T. Mirea, B. Díaz-Durán, M. Clement, M. DeMiguel-Ramos, J. Sangrador, J. de Frutos, and E. Iborra, *Carbon* 90, 9 (2015).
- 31 L. Rosenberger, R. Baird, E. Mc Cullen, G. Auner, and G. Shreve, *Surf. Interface Anal.* 40, 1254 (2008).
- 32 F. Malengreau, V. Hautier, M. Vermeersch, R. Sporken, and R. Caudano, *Surf. Science*, 330, 75 (1995).
- 33 R. Brajpuriya and T. Shripathi, *Appl. Surf. Science* 255, 6149 (2009).
- 34 G. Klopman, *J. Chem. Phys.* 43, S124 (1965).
- 35 T. Yamabe, K. Hori, T. Minato, and K. Fukui, *Inorg. Chem.* 19, 2154 (1980).
- ³⁶ X. Li, A. Cuo, Y. J. Jung, R. Vajtai, and P. M. Ajayan, *Nano Lett.* 5, 1997 (2005).